VEHICLE SYSTEM DYNAMICS
https://doi.org/10.1080/00423114.2025.2471346

OPEN ACCESS Check for updates

Post-critical behaviour of the powerslide motion

Johannes Edelmann, Manuel Eberhart, Alois Steindl and Manfred Plöchl

Institute of Mechanics and Mechatronics, TU Wien, Vienna, Austria

ABSTRACT

It is a challenge to control the vehicle motion when tyre forces at the rear axle are saturated and the sideslip angle of the vehicle is large. At the steady-state cornering condition called powerslide or drifting, the front wheels are steered to the outside of the curve, and the corresponding equilibrium is unstable. While previous and ongoing research concentrates above all on different stabilisation approaches, the post-critical behaviour is given attention in this study. Based on the nonlinear system equations of a basic two-wheel vehicle and brush tyre model, it is found that for a range of constant steering angles and constant drive torques at the rear driven wheels, the vehicle motion and states converge to a steady-state with a small radius of curvature or to a stable limit cycle orbiting an unstable equilibrium.

ARTICLE HISTORY
Received 15 June 2024
Revised 9 December 2024
Accepted 7 February 2025

KEYWORDS
Loss of stability; bifurcation; vehicle handling behaviour; stability of motion; powerslide; drifting

1. Introduction

Pushing vigorously the accelerator pedal of a rear-wheel drive (RWD) vehicle during cornering reduces the lateral forces of the rear axle. The resulting change of yaw moment then turns the vehicle's longitudinal axis towards the inside of the corner, causing a large sideslip angle of the vehicle. The driver may now balance the motion by steering the front wheels to the outside of the corner, called countersteer. The established equilibrium is a possible solution of steady-state cornering and is called powerslide motion, [1], or simply drifting.

It is found in [2] that the existence of the powerslide motion is above all a phenomenon of the tyre characteristics, in particular of the degressive behaviour of the lateral forces at large longitudinal slip. Linearisation of the nonlinear equations of motion of a RWD vehicle and tyre model reveals that the powerslide equilibrium is unstable, [2]. Analysis of the eigenvector related to the positive real (and therefore unstable) eigenvalue shows a strong coupling between the longitudinal and the lateral vehicle states, [3,4].

It is reported in [5] that the unstable powerslide equilibrium, derived from a 3-DOF vehicle model, including longitudinal velocity, lateral velocity, and yaw rate, is a saddle point with characteristics that exhibit low sensitivity to friction potential and speed variation. At the powerslide equilibrium, non-minimum phase characteristics appear between steering angle and vehicle sideslip angle, which could facilitate destabilisation due to the right half zero, [6]. Therefore it is suggested to better control vehicle sideslip by controlling

CONTACT Johannes Edelmann johannes.edelmann@tuwien.ac.at

the yaw rate or even by applying longitudinal control that allows also to sustain a drifting motion. In [4] it is found from controllability analysis that the control of the rear wheel torque is very effective in stabilising the powerslide motion, which can also be observed from the power thrusts of the driver when drifting.

While the stabilisation of the unstable powerslide equilibrium, either fully autonomously, [7–11], by the driver, [12], or with shared control, [13], has drawn a lot of attention by researchers, only little attention has been given to the dynamics of the vehicle after loss of stability with fixed control inputs. Therefore, this paper aims to close this gap and contribute to a better understanding of the post-critical behaviour of the powerslide motion. It builds on the conference paper [14] of the authors.

The remainder of this paper is organised as follows: Section 2 introduces the applied vehicle model with RWD and the tyre model used to map the nonlinear tyre characteristics. In Section 3 the post-critical behaviour is studied. Therefore, the vehicle motion after loss of stability is illustrated, the handling diagram focussing the powerslide branch is analysed in detail, and a bifurcation analysis is performed and discussed to outline and explain the resulting periodic vehicle motion. Measurement results that support the theoretical findings are included as well. Finally, the main outcome of the paper is summarised, and conclusions are drawn.

2. Tyre and vehicle model

A two-wheel vehicle model with RWD is used to map the powerslide motion and the dynamic behaviour after loss of stability. This model is particularly reasonable at low-friction surfaces when the load transfer between the left and the right wheels is less important and may thus be neglected. The vehicle model in powerslide condition is plotted in Figure 1. The velocity v, the sideslip angle β of the vehicle and the yaw rate $\dot{\psi}$ constitute, together with the angular velocity ω_R of the rear wheel, the state variables of the system. The system control inputs are the steering angle δ_F of the front wheel and the drive torque M_R at the rear wheel.

The nonlinear equations of motion of the vehicle and the rear wheel are

$$m\dot{v}\cos\beta - m(\dot{\psi}+\dot{\beta})v\sin\beta = F_{xR} - F_{yF}\sin\delta_F, \tag{1a}$$

$$m\dot{v}\sin\beta + m(\dot{\psi}+\dot{\beta})v\cos\beta = F_{yR} + F_{yF}\cos\delta_F, \tag{1b}$$

$$I_z\ddot{\psi} = F_{yF}\cos\delta_F\, l_F - F_{yR}\, l_R, \tag{1c}$$

$$I_w\dot{\omega}_R = M_R - F_{xR}\, r_l, \tag{1d}$$

with vehicle mass m, yaw moment of inertia I_z of the vehicle, moment of inertia I_w of the rear axle, the distances l_F and l_R from the centre of gravity (COG) to the front, and to the rear axle, respectively, and the loaded radius r_l of the rear wheel.

Also for the sake of simplicity, the brush tyre model from [15] is chosen to represent the tyre characteristics, including typically less realistic assumptions, such as the same lateral and longitudinal tyre slip stiffness. The horizontal tyre forces F_{yF}, F_{xR}, F_{yR} depend on the sideslip angles α_i, the longitudinal slips κ_i, and the vertical tyre loads F_{zi} with $i = F, R$. The normalised steady-state tyre/axle characteristics are shown in Figure 2 for the theoretical slips $\sigma_{xi} = \kappa_i/(1+\kappa_i)$ and $\sigma_{yi} = \tan\alpha_i/(1+\kappa_i)$, see Appendix. The characteristics of the

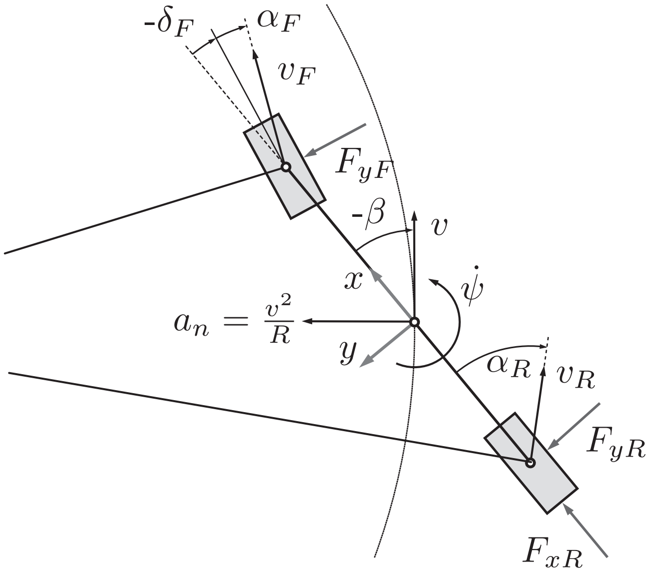

Figure 1. Powerslide driving condition for rear-wheel drive vehicle model.

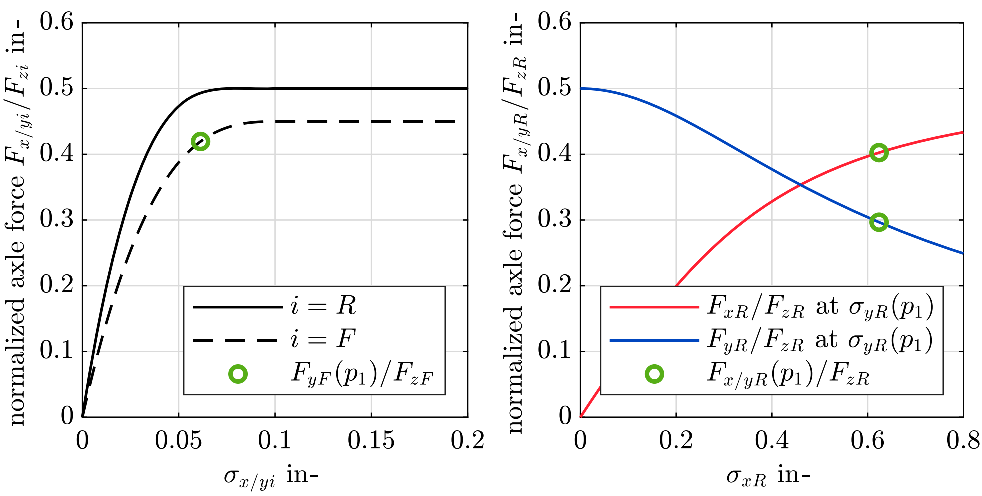

Figure 2. Normalised tyre/axle characteristics with marked normalised tyre/axle forces at powerslide equilibrium p_1.

front and the rear tyre/axle are different and result in a slightly understeer vehicle, see later Figure 3. On the left of Figure 2 the 'stronger' rear axle with respect to the front axle can be noticed. For the same constant sideslip angle, the decrease of the rear lateral axle force with increasing longitudinal slip is presented on the right, and the corresponding tyre/axle forces associated with the later addressed powerslide equilibrium p_1 are marked.

The parameters used for the numeric results in Section 3 are listed in Table 1.

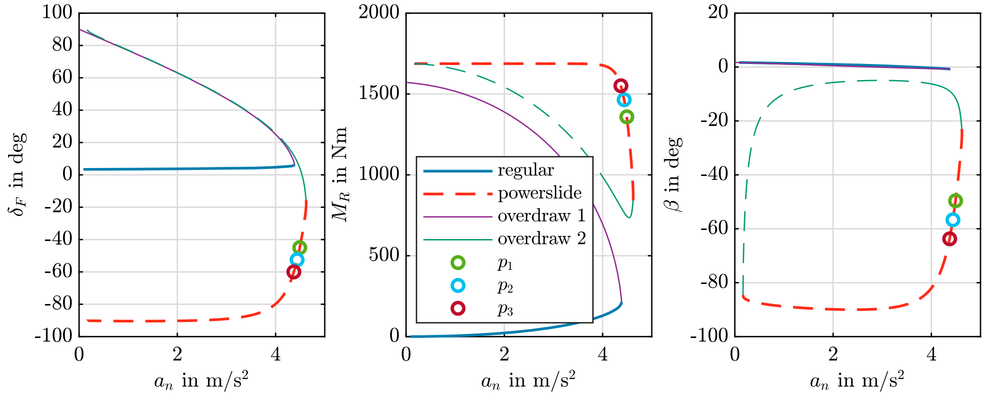

Figure 3. Handling diagram with regular driving and powerslide branch for constant radius (50 m) cornering (solid lines: stable solutions; dashed line: unstable solutions).

Table 1. Parameters of the two-wheel vehicle and tyre/axle model.

parameter	symbol	value	unit
vehicle mass	m	2000	kg
yaw inertia of inertia	I_z	2650	kg m^2
moment of inertia of rear axle	I_w	6	kg m^2
distance of COG to front axle	l_F	1.45	m
distance of COG to rear axle	l_R	1.50	m
loaded radius of rear wheel	r_l	0.35	m
effective rolling radius of rear tyre	r_e	0.35	m
front tyre/axle slip stiffness	$2c_{pF}a_F^2$	$9{\cdot}10^4$	N
rear tyre/axle slip stiffness	$2c_{pR}a_R^2$	$6.5{\cdot}10^4$	N
max. friction coefficients	μ_F, μ_R	0.45, 0.5	–

3. Stability of powerslide equilibrium and post-critical dynamic behaviour

The required steering angle, drive torque at the rear axle and vehicle sideslip angle for quasi-steady-state cornering at a constant radius of 50 m are shown in the handling diagram in Figure 3. Besides the equilibria of the regular driving branch and the powerslide branch, overdraw solutions, which are not relevant in this context, are depicted. Note that slightly larger normal accelerations can be reached in powerslide motion. The requested drive torque is larger than for regular driving, thus the powerslide motion is less energy-efficient.

The required drive torque at the rear axle in powerslide motion increases in a quite proportional manner with steering angle within the range of practical interest, Figure 4, which can be useful information for the human driver to control the powerslide. The powerslide equilibria p_1, p_2, and p_3 marked in Figures 3 and 4 are analysed below w.r.t. the corresponding post-critical behaviour in detail.

Now, the system equations are linearised at the equilibria on the powerslide branch. The resulting four eigenvalues and corresponding eigenvectors for varied normal accelerations are shown in Figure 5, with equilibrium p_1 marked again. The positive eigenvalue, red line, reveals the unstable nature of the powerslide branch and its eigenvector the relatively strong coupling of the generalised coordinates in longitudinal (v, ω_R) and lateral ($\dot{\psi}$, β)

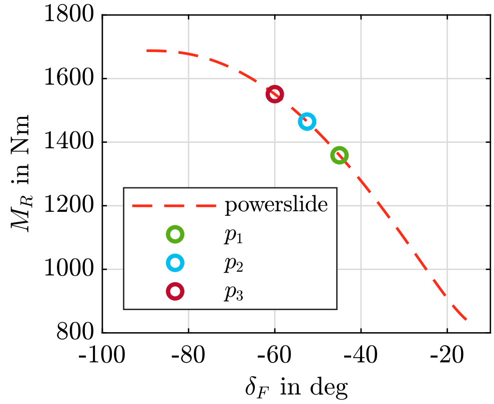

Figure 4. Relationship between the steering angle and the rear drive torque corresponding to Figure 3 for the (unstable) powerslide branch.

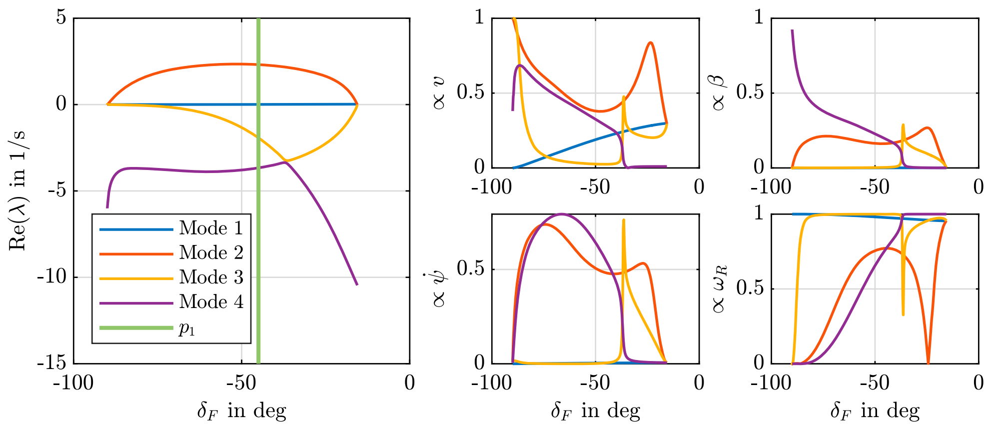

Figure 5. Eigenvalues and corresponding eigenvectors corresponding to Figure 3 for the powerslide branch.

directions. The results are similar to [4], where a four-wheel vehicle model and a detailed tyre model are applied.

As the positive eigenvalue is real, a monotonic loss of stability, with the vehicle spinning in or out, can be expected to appear. But interestingly, simulations of the vehicle motion after loss of stability at a wide range of powerslide equilibria show that the vehicle will end up in flower-like, periodic motions, see trajectories in Figure 6, for fixed control inputs. Drivers may know this phenomenon from their own experience when they keep both the steering angle and accelerator pedal fixed and draw tyre marks on the surface. The green flower refers again to the green powerslide equilibrium p_1, and the other trajectories to the powerslide equilibria marked in the handling diagram in Figure 3 and the relationship between steering angle and drive torque in Figure 4 with p_2 and p_3.

The COG of the vehicle may deviate to the inside or the outside of the circle closely after a loss of stability. The following approach may be applied to decide about the direction, and it is illustrated in an example.

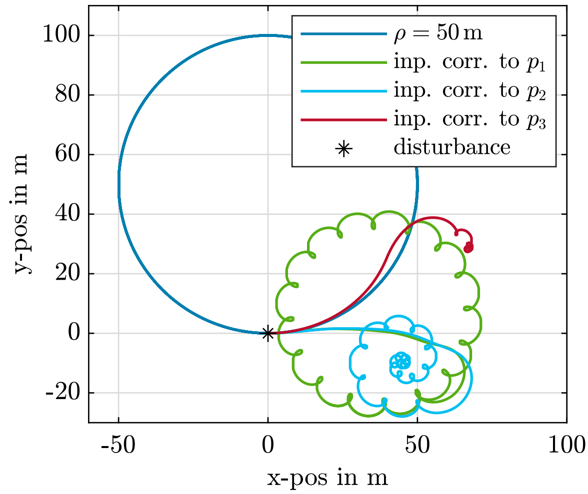

Figure 6. Trajectories of the COG of the vehicle after loss of stability at powerslide equilibria p_1, p_2, p_3 and initial trajectories referring to a given disturbance at position '$*$' addressed in the *Example*.

For the considered powerslide branch, a pair of unstable complex conjugate eigenvalues and two real eigenvalues, with one unstable, appear, Figure 5. This positive real eigenvalue will govern the evolution of the system (1) with state vector

$$\boldsymbol{x} = [v, \beta, \dot{\psi}, \omega_R]^T. \tag{2}$$

The powerslide equilibrium is denoted with state vector $\boldsymbol{x}_0$, and the radius of the traced circle is

$$\varrho = v/\dot{\psi}. \tag{3}$$

If the initial state vector $\boldsymbol{x}(0)$ is given by

$$\boldsymbol{x}(0) = \boldsymbol{x}_0 + \varepsilon \boldsymbol{v}_u, \tag{4}$$

where $\boldsymbol{v}_u$ denotes the eigenvector corresponding to the dominant unstable eigenvalue λ_u, the trajectory will evolve initially according to

$$\boldsymbol{x}(t) = \boldsymbol{x}_0 + \exp(\lambda_u t)\varepsilon \boldsymbol{v}_u. \tag{5}$$

For $\varrho(t)$ one obtains the relation

$$\dot{\varrho} = \frac{\dot{v}\dot{\psi} - v\ddot{\psi}}{\dot{\psi}^2}. \tag{6}$$

With $\dot{\boldsymbol{x}}(0) = \lambda_u \varepsilon \boldsymbol{v}_u$ there follows

$$\dot{\varrho}(0) = \lambda_u \varepsilon \frac{v_{u,1}\dot{\psi}(0) - v(0)v_{u,3}}{\dot{\psi}^2(0)}, \tag{7}$$

where $v_{u,k}$ denotes the kth component of $\boldsymbol{v}_u$. For $\dot{\varrho}(0) > 0$, the circle will grow initially.

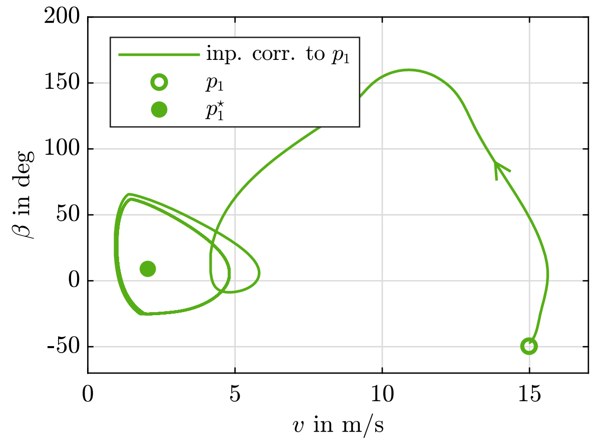

Figure 7. Trajectory in the (v, β)-phase plane after loss of stability: from (disturbed) powerslide equilibrium p_1 towards encircling the unstable equilibrium $p_1^\star$.

If the initial state $\boldsymbol{x}(0)$ lies close to the powerslide equilibrium state $\boldsymbol{x}_0$, its component in the dominating unstable direction is given by the projection of $\boldsymbol{d}_0 = \boldsymbol{x}(0) - \boldsymbol{x}_0$ into the direction of $\boldsymbol{v}_u$. If

$$\mathbf{V} = [\boldsymbol{v}_1, \boldsymbol{v}_2, \ldots, \boldsymbol{v}_n = \boldsymbol{v}_u]$$

denotes the matrix of eigenvectors with $\boldsymbol{v}_u$ in the last column, the coefficient c_u of $\boldsymbol{d}_0$ w.r.t. the eigenvector basis is given by

$$c_u = \boldsymbol{W}_n \boldsymbol{d}_0, \tag{8}$$

where $\boldsymbol{W}_n$ denotes the last line of $\mathbf{W} = \mathbf{V}^{-1}$. This follows from the relation $\boldsymbol{d}_0 = \mathbf{V}\boldsymbol{c}$. The calculation of the inverse matrix may be avoided by using the left eigenvectors. c_u is then used for ε in (7).

Now, as an *Example*, a disturbance $\Delta\beta = \pm 3^\circ$ of the sideslip angle of the vehicle with respect to its steady-state value in powerslide motion with equilibria p_1, p_2 and p_3 is considered at an arbitrary time instant $t = 0$. The resulting initial trajectories are included in Figure 6. For $\Delta\beta = -3^\circ$, the vehicle will leave the circle to the outside after loss of stability, green and blue trajectory. In contrast, for $\Delta\beta = 3^\circ$, the vehicle will turn inside, red trajectory in Figure 6.

Looking at the green trajectory of the COG in the x-y-plane in Figure 6 and at the green trajectory in the (v, β)-phase plane starting from the (disturbed) equilibrium p_1 in Figure 7 suggests that the trajectories converge to a stable periodic solution encircling a further equilibrium $p_1^\star$.

This equilibrium $p_1^\star$ coexists with the stationary equilibrium p_1 for the same control inputs. Deriving further $p_i^\star$ corresponding to respective p_i on the powerslide branch, by using the continuation method MATCONT, [16], results in a new branch that is depicted on the top plot in Figure 8 by the black line. The equilibria $p_i^\star$ on this branch undergo Hopf bifurcations at the Hopf points H_1 and H_2. In between, stable limit cycles evolve.

From the above, it becomes clear that after the monotonic loss of stability at the powerslide equilibrium, the motion finally results in a stable periodic motion. The three pairs

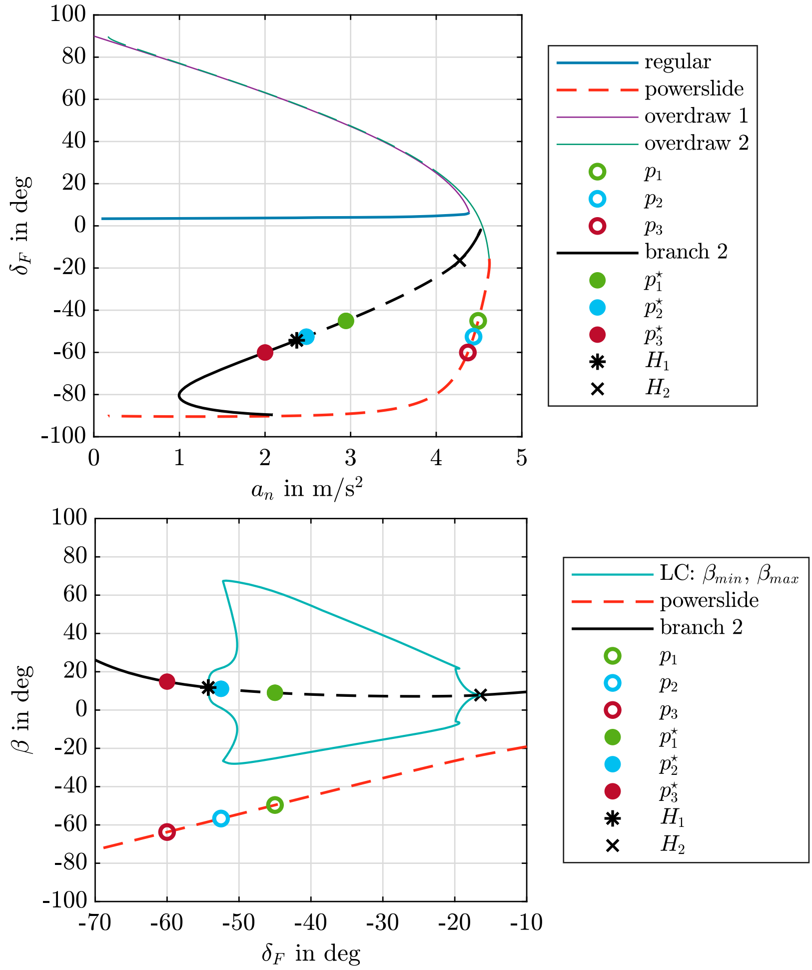

Figure 8. Handling and bifurcation diagram (solid lines: stable solutions; dashed line: unstable solutions).

of equilibria, p_j and $p_j^\star$, $j = 1$-3, are included in the handling diagram and the respective branch of the bifurcation diagram at the bottom plot of Figure 8, with the steering angle as the bifurcation parameter. The bifurcation diagram depicts the maximum and minimum values of the sideslip angles of the vehicle at the limit cycles. With increasing (negative) steering angle, the branch of unstable equilibria $p_i^\star$ turns stable at Hopf point H_1. This is interesting to note, as for very large (negative) steering angles (and large drive torques, Figure 4), even a stable, stationary solution ($p_3^\star$) as a circular trajectory with a small radius of curvature on the x-y-plane may appear (and may be noticed as 'donut' marks on the surface). Figure 9 shows these small radii of the solutions, in particular when they turn stable after the Hopf point H_1. While the regular driving and powerslide equilibria are related to the given radius of 50 m in the handling diagram at the top plot of Figure 8, the graph with equilibria $p_i^\star$ is related to the varying radii presented in Figure 9.

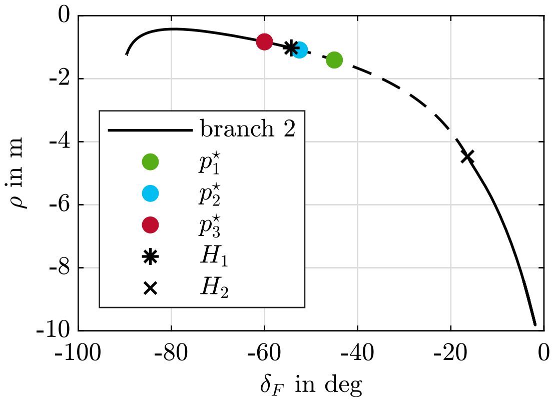

Figure 9. Bifurcation diagram with the steering angle δ_F as bifurcation parameter for the radius of curvature ϱ (solid lines: stable solutions; dashed line: unstable solutions).

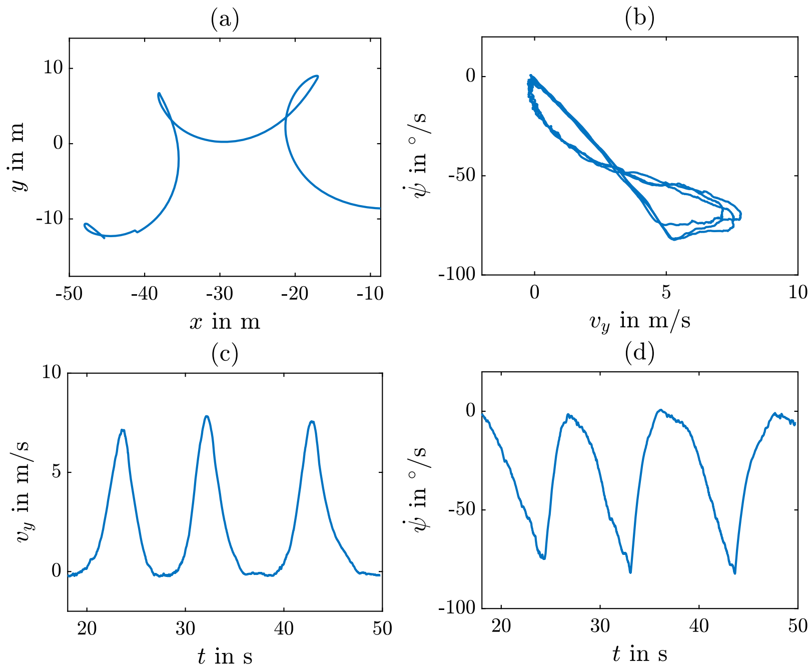

Figure 10. Measured signals of the vehicle motion after loss of stability with fixed control inputs $\delta_F \approx -9^\circ$ and $M_R \approx 1000$ Nm: (a) trajectory of COG in x-y-plane; (b) ($\dot{\psi}$,v_y)-phase plane; (c) yaw rate $\dot{\psi}(t)$; (d) lateral velocity $v_y(t)$.

To confirm the occurrence of a periodic motion after the loss of stability with fixed control inputs, also respective vehicle tests were carried out. The tests were performed on packed snow with an SUV-type electric vehicle with a motor at the front axle and a motor at the rear axle with locked differential. Actually for other test purposes, the motor torques could be controlled freely. To mimic an RWD vehicle, the front axle motor torque was set to a minimum, and the rear axle torque was controlled to achieve a demanded torque. Next

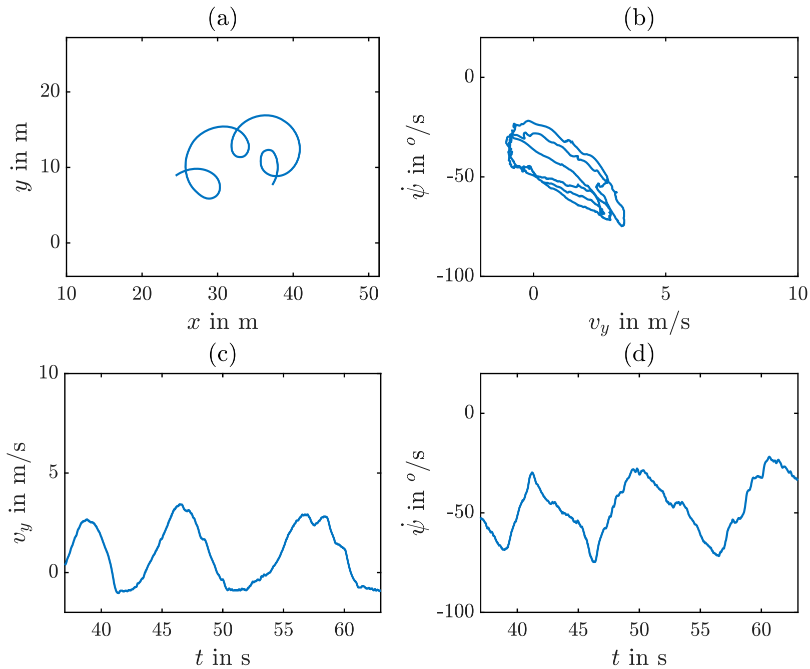

Figure 11. Measured signals of the vehicle motion after loss of stability with fixed control inputs $\delta_F \approx -38^\circ$ and $M_R \approx 1350$ Nm: (a) trajectory of COG in x-y-plane; (b) ($\dot{\psi}$,v_y)-phase plane; (c) yaw rate $\dot{\psi}(t)$; (d) lateral velocity $v_y(t)$.

to the signals on the vehicle data bus, a high-precision dual antenna GNSS-aided Inertial Measuring Unit (GNSS-IMU) was available as a measuring system in particular for the lateral velocity of the vehicle. Winter tyres of different dimensions were mounted on the front and rear axles. The vehicle and tyre/road friction parameters match only roughly to the parameters given in Table 1.

The test manoeuvres were initiated when the driver (continuously) fully pushed the accelerator pedal, which allowed the torque control to modulate the torque request and set a demanded value while the driver countersteered for stabilisation in the initial phase and then kept the steering hand wheel fixed in approximate powerslide motion.

Figures 10 and 11 show the measured results of two of the test manoeuvres. While the first manoeuvre relates to a powerslide motion with a small steering and vehicle sideslip angle, the second manoeuvre relates to large angles. As model parameters and parameters of the test condition are different to some extent, the measurement results correspond only roughly to the above derived characteristics. Nevertheless, the graphs reveal that the vehicle indeed runs into limit cycles in both test manoeuvres, which becomes most obvious from the trajectories in the ($\dot{\psi}$,v_y)-phase plane in (b) and the periodic time histories of the yaw rate $\dot{\psi}(t)$ in (c) and the lateral velocity $v_y(t) = v(t)\sin\beta(t)$ in (d). Also, flower-like trajectories of the COG in the x-y-plane appear, see (a). The vehicle had to be stopped (e.g. on the left side of the plot (a) in Figure 10), and so the drawing of a full flower due to limited space. The centre of the unstable equilibrium cannot be spotted anyway because of naturally occurring (e.g. frictional) disturbances on the one hand and the unstabilised vehicle states on the other hand. For the test manoeuvre with the large steering angle, Figure 11, the periodicity is more disturbed than in Figure 10 but still evident.

4. Conclusions

The loss of stability of a vehicle in powerslide motion (i.e. when drifting) is of monotonic nature due to a typically dominant positive real eigenvalue of the system, linearised w.r.t. the powerslide equilibrium. The yaw rate of the vehicle will start to increase or decrease depending on the disturbance. Then, there will be a transition from the powerslide equilibrium to another equilibrium for the same fixed controls. For very large (negative) steering angles, this equilibrium may be stable, and the vehicle will end again in steady-state cornering with a typically small radius, but with different states compared to the corresponding steady-state cornering in powerslide condition. For smaller steering angles, the equilibrium will be unstable and of oscillatory nature and a respective Hopf bifurcation is found. The resulting stable limit cycles of the vehicle states appear as flower-like trajectories on the road plane, where the COG of the vehicle spirals around a fixed point.

While recent studies mainly focus on controlling or stabilising the powerslide, the loss of stability and its consequences still needed to be addressed. The findings in this paper build on theoretical research, but evidence from practical observations and first vehicle test runs suggests the plausibility of the results.

From a practical application point of view, trajectories of the COG and vehicle states in the time period (closely) after the loss of stability seem to be most important, as the powerslide and related trajectories that would not be feasible with regular driving are becoming more relevant in recent and future research, e.g. [11].

Acknowledgments

We acknowledge TU Wien Bibliothek for financial support through its Open Access Funding Program.

Disclosure statement

No potential conflict of interest was reported by the author(s).

ORCID

Alois Steindl http://orcid.org/0000-0002-6813-2486

References

[1] Edelmann J, Plöchl M, Lugner P, et al. Investigations on the powerslide of automobiles. In: 9th International Symposium on Advanced Vehicle Control (AVEC'08); 2008 Oct 6–9; Kobe, Japan. Available from: https://repositum.tuwien.at/handle/20.500.12708/65776.

[2] Edelmann J, Plöchl M. Handling characteristics and stability of the steady-state powerslide motion of an automobile. Regul Chaotic Dyn. 2009;14(6):682–692. doi: 10.1134/S1560354709060069.

[3] Edelmann J, Plöchl M. Controllability of the powerslide motion of an automobile with different actuation inputs. PAMM. 2016;16:803–804. doi: 10.1002/pamm.201610390.

[4] Edelmann J, Plöchl M. Controllability of the powerslide motion of vehicles with different drive concepts. Procedia Eng. 2017;199:3266–3271. doi: 10.1016/j.proeng.2017.09.357.
[5] Hindiyeh RY, Gerdes JC. Equilibrium analysis of drifting vehicles for control design. In: ASME 2009 Dynamic Systems and Control Conference; 2009 Oct 12–14; Hollywood, California, USA. p. 181–188.
[6] Voser C, Hindiyeh RY, Gerdes JC. Analysis and control of high sideslip manoeuvres. Veh Syst Dyn. 2010;48(sup1):317–336. doi: 10.1080/00423111003746140.
[7] Werling M, Reinisch P, Gröll L. Robust power-slide control for a production vehicle. Int J Veh Auton Syst. 2015;13(1):27–42. doi: 10.1504/IJVAS.2015.070727.
[8] Goh JY, Gerdes JC. Simultaneous stabilization and tracking of basic automobile drifting trajectories. In: 2016 IEEE Intelligent Vehicles Symposium (IV); 2016; Gothenburg, Sweden. p. 597–602.
[9] Vignati M, Sabbioni E, Cheli F. A torque vectoring control for enhancing vehicle performance in drifting. Electronics. 2018;7(12):394. doi: 10.3390/electronics7120394.
[10] Goh JY, Goel T, Gerdes JC. Toward automated vehicle control beyond the stability limits: drifting along a general path. J Dyn Syst-T Asme. 2020;142(2):Article ID 021004. doi: 10.1115/1.4045320
[11] Stano P, Tavernini D, Montanaro U, et al. Enhanced active safety through integrated autonomous drifting and direct yaw moment control via nonlinear model predictive control. IEEE Trans Intell Veh. 2023;9(2):4172–4190. doi: 10.1109/TIV.2023.3340992.
[12] Edelmann J, Plöchl M, Pfeffer P. Analysis of steady-state vehicle handling and driver behaviour at extreme driving conditions. In: Proceedings of 22st International Symposium on Dynamics of Vehicles on Roads and Tracks (IAVSD 2011); 2011; Manchester, UK. Available from: https://repositum.tuwien.at/handle/20.500.12708/66338.
[13] Eberhart M, Plöchl M, Unterreiner M, et al. Insights into stability and control of the powerslide motion with variable drive torque distribution – applied to a driver assistance system. Veh Syst Dyn. 2025;1–21. doi: 10.1080/00423114.2025.2457433.
[14] Steindl A, Edelmann J, Plöchl M. Influence of tyre characteristics on periodic motions for an understeering vehicle. PAMM. 2023;22(1):e202200289. doi: 10.1002/pamm.202200289.
[15] Pacejka HB. Tire and vehicle dynamics. 3rd ed. Oxford Waltham: Butterworth-Heinemann Elsevier; 2012.
[16] Dhooge A, Govaerts W, Kuznetsov YA. MatCont: a matlab package for numerical bifurcation analysis of ODEs. ACM Trans Math Softw. 2003;29(2):141–164. doi: 10.1145/779359.779362.

Appendix. Tyre model

The brush tyre model in [15] is applied for the front and rear tyre characteristics. Here, the model equations for the rear tyre are given in a compact manner; the model equations for the front tyre are similar but 'pure lateral'. In contrast to [15], no practical slips κ and $\tan\alpha$ are introduced, but the theoretical slips,

$$\sigma_{xR} = -\frac{v_{sxR}}{|r_e\omega_R|}, \quad \sigma_{yR} = -\frac{v_{syR}}{|r_e\omega_R|}, \quad \sigma_R = \sqrt{\sigma_{xR}^2 + \sigma_{yR}^2}, \tag{A1}$$

with longitudinal and lateral slip velocities v_{sxR} and v_{syR},

$$v_{sxR} = v\cos\beta - r_e\omega_R \quad \text{and} \quad v_{syR} = v\sin\beta - l_R\dot{\psi}, \tag{A2}$$

are directly related to the kinematics of the vehicle model. Then, the magnitude of the rear tyre/axle force F_R reads

$$F_R = \begin{cases} \mu_R F_{zR}(3\theta_R\sigma_R - 3(\theta_R\sigma_R)^2 + (\theta_R\sigma_R)^3) & \text{for } \sigma_R \le \sigma_{\mathrm{sl}\,R} \\ \mu_R F_{zR} & \text{for } \sigma_R > \sigma_{\mathrm{sl}\,R} \end{cases} \tag{A3}$$

with slip $\sigma_{\mathrm{sl}\,R} = 1/\theta_R$ where total sliding starts and parameter

$$\theta_R = \frac{2c_{pR}a_R^2}{3\mu_R F_{zR}}. \tag{A4}$$

Finally, the longitudinal and lateral components of the rear tyre/axle force are

$$F_{xR} = F_R\frac{\sigma_{xR}}{\sigma_R} \quad \text{and} \quad F_{yR} = F_R\frac{\sigma_{yR}}{\sigma_R}. \tag{A5}$$